GEM - International Journal on Geomathematics

Validation of an upscaled poroelasticity formulation for high-aspect ratio geological structures such as fractures and faults

--Manuscript Draft--

Manuscript Number:	IJGE-D-22-00003
Full Title:	Validation of an upscaled poroelasticity formulation for high-aspect ratio geological structures such as fractures and faults
Article Type:	Original Paper
Corresponding Author:	Tore Ingvald Bjørnarå, Ph.D. Norwegian Geotechnical Institute Oslo, NORWAY
Corresponding Author Secondary Information:	
Corresponding Author's Institution:	Norwegian Geotechnical Institute
Corresponding Author's Secondary Institution:	
First Author:	Tore Ingvald Bjørnarå, Ph.D.
First Author Secondary Information:	
Order of Authors:	Tore Ingvald Bjørnarå, Ph.D.
	Joonsang Park
	Bahman Bohloli
Order of Authors Secondary Information:	
Funding Information:	ERA-NET ACT (691712) — Dr. Bahman Bohloli Gassnova (299664) — Dr. Bahman Bohloli

Abstract:

In regional-scale processes, such as CO2 storage and reservoir pressure support during hydro-carbon production, small-scale structures like fractures and faults can in results in large numerical problems that renders a numerical solution infeasible. To numerically resolve and solve such thin features we need to resort to averaging and upscaling techniques. Here we describe the poroelastic response in a high-aspect ratio structure by using dimensional reduction via a zero-thickness element type. The governing equations are integrated across the thickness of the high-aspect ratio domain, assuming linear variation in displacement across the thickness of the structure, to derive a traction force on the upscaled structure termed poroelastic normal deflection equation (PND). The solution of the PND approximation is compared, in a Monte Carlo simulation study, to a typically used Goodman-type upscaling approximation (thin elastic layer, TEL) as well as a reference solution where the high-aspect ratio structure is fully resolved. The PND formulation is here demonstrated in a finite element method framework. It was found that the PND is robust with an accuracy that is to a leading order depending on the thickness, or aspect ratio, of the upscaled structure. For an aspect ratio of 5 %, the error, compared to the reference solution, is generally less than 10 %. The accuracy of TEL is to a leading order depending on the stiffness ratio between the upscaled structure and the surrounding formations. The error when using TEL is lower or equal compared to PND for soft upscaled structures, but the accuracy breaks down when the surrounding formations become softer than the upscaled structure (error up to 1000 times larger compared to PND). The robustness and generally elevated accuracy of PND compared to TEL is due to the addition of extra degrees of freedom, but the added numerical cost is very modest since it only applies to the already dimensionally reduced domain. Furthermore, PND requires only a minor modification to any numerical code that already supports TEL, making PND more attractive to use.

Validation of an upscaled poroelasticity formulation for high-aspect ratio geological structures such as fractures and faults

Tore Ingvald Bjørnarå[1,*], Joonsang Park[1], Bahman Bohloli[1]

[1]Norwegian Geotechnical Institute, Oslo, Norway

*E-mail corresponding author: tore.ingvald.bjornara@ngi.no

Keywords: poroelasticity, high-aspect ratio, upscaling, zero-thickness element

1 Abstract

In regional-scale processes, such as CO2 storage and reservoir pressure support during hydro-carbon production, small-scale structures like fractures and faults can in results in large numerical problems that renders a numerical solution infeasible. To numerically resolve and solve such thin features we need to resort to averaging and upscaling techniques. Here we describe the poroelastic response in a high-aspect ratio structure by using dimensional reduction via a zero-thickness element type. The governing equations are integrated across the thickness of the high-aspect ratio domain, assuming linear variation in displacement across the thickness of the structure, to derive a traction force on the upscaled structure termed poroelastic normal deflection equation (PND). The solution of the PND approximation is compared, in a Monte Carlo simulation study, to a typically used Goodman-type upscaling approximation (thin elastic layer, TEL) as well as a reference solution where the high-aspect ratio structure is fully resolved. The PND formulation is here demonstrated in a finite element method framework. It was found that the PND is robust with an accuracy that is to a leading order depending on the thickness, or aspect ratio, of the upscaled structure. For an aspect ratio of 5 %, the error,

compared to the reference solution, is generally less than 10 %. The accuracy of TEL is to a leading order depending on the stiffness ratio between the upscaled structure and the surrounding formations. The error when using TEL is lower or equal compared to PND for soft upscaled structures, but the accuracy breaks down when the surrounding formations become softer than the upscaled structure (error up to 1000 times larger compared to PND). The robustness and generally elevated accuracy of PND compared to TEL is due to the addition of extra degrees of freedom, but the added numerical cost is very modest since it only applies to the already dimensionally reduced domain. Furthermore, PND requires only a minor modification to any numerical code that already supports TEL, making PND more attractive to use.

2 Introduction

Regional-scale models are central when studying the performance of large-scale subsurface processes such as CO2 storage, reservoir pressure support during hydro-carbon production and others. In regional-scale models it is often necessary to include details of a formation or a geological feature where one of the dimensions are relatively thin compared to the characteristic length or width scale of the feature or area of interest. These features are known as high-aspect ratio geometric shapes or entity and may even be shown as lines on geological maps and seismic interpretations. Such thin features can be structures such as faults, fractures and dikes, or even stratigraphic units, e.g., thin reservoirs and caprocks.

The thin nature of a high-aspect ratio geometric entity adds details to the numerical description of a model. When discretizing details in a numerical model (e.g., finite element, finite difference), the resolution increases with the level of details, e.g., increases the computational grid/mesh density. This increase in resolution may not be an issue in two dimensional models, but in three dimensional models, it rapidly increases the computational demand, to the point that full three-dimensional descriptions are rendered infeasible. These high-aspect ratio entities, although shown as lines on geological maps and seismic interpretations, can also have complex internal structures and may dominate the hydromechanics of reservoir or caprock, consider for example geocellular description of a fault structure (Fredman et al., 2007; Kolyukhin and Tveranger, 2015; Grant, 2020; Bjørnarå et al., 2021). This leads us to search for simplifications that do not significantly alter the problem and the solution.

One remediation is to simply ignore some or all the high-aspect ratio entities (defeaturing) or simplify the morphology of the structure. In the case of faults in geocellular models (e.g., Lutome et al., 2021) and geocellular faults (e.g., Fredman et al., 2007), representing another remediation, is that the along-fault flow process is sometimes completely ignored such that the property of a complex fault is reduced to a pressure discontinuity in the across-fault flow direction only, characterised by transmissibility multipliers. Both approaches are sometimes good and appropriate approximations, because reducing details is always a good strategy, but when reducing too much then also too much information may be lost, and when reducing too little the model can be too demanding to solve.

Another, more attractive method, in line with the latter transmissibility multiplier, is the use of upscaling techniques where a rock body or structure, is reduced to a zero-thickness surface. Upscaling can be done in several ways. Here we consider dimensional reduction, of a high-aspect ratio (HAR) geometrical entity, that together with the appropriate mathematical description, substantially reduces the size of the numerical problem while retaining the accuracy. This benefit has historically been demonstrated extensively for fluid flow, both single-phase and multi-phase flow, a.k.a. segregated flow and Dupuit approximation, with a renewed interest to simulate regional-scale CO_2 migration (e.g., Nordbotten et al., 2005; Gasda et al., 2011). To capture the geomechanical response in thin layers, spring descriptions have been used, where a high-aspect ratio entity is replaced by a discontinuity with springs representing stiffness in normal direction and tangential (shear) direction (e.g., Goodman et al., 1968). Instead, here we apply a more detailed description, a zero-thickness element type approach with a linearized description of the displacement components across the thickness of the reduced domain. This approximation, termed poroelastic normal deflection (PND), was inspired by early works by Bear and Corapcioglu (1981a, 1981b, 1983) which was extended to also consider varying horizontal displacement and embedded volumes. The PND approximation was validated in 2D for an embedded horizontal domain (Bjørnarå et al., 2016) and applied to a vertical fault structure in combination with the cohesive zone model (e.g., Camanho and Hallet, 2015) for a vertical domain (Bjørnarå et al., 2021).

The PND approximation allows replacing relatively thin structures with variable thickness and shape to substantially reduce the complexity of a numerical model and the method is flexible and extendable to also capture more complex internal structure, e.g., multiple and/or heterogeneous layers. The mathematical description of PND is described and the aim of this paper is to demonstrate its applicability through a validation study where the results of using PND and a commonly used upscaling technique are compared to the results from a full-dimensional model.

In the following we will use abbreviations to distinguish the two upscaling methods applied here. *PND* is a zero-thickness thin-layer element that will be compared to the simpler Goodman-type interface element that will be referred to as *TEL* (thin elastic layer). *HAR* geometrical entity is a high-aspect ratio volume domain that is, in the PND and TEL approach, collapsed to a surface domain. By *upscaled* *structure* we here mean a volumetric structure that is collapsed to a lower dimensional object (a face/surface in 3D, and an edge in 2D) such that it has zero thickness.

3 Method

To validate the PND approximation we need to upscale the poroelasticity equations and first we define the governing equations for linear poroelasticity of a porous media as described by Biot (1941). These equations require special treatment in the upscaled structure, which is to solve on a zero-thickness domain, obtained by integrating the governing equations across the thickness of the weakness zone. Poroelasticity describes the constitutive behaviour of a fluid saturated rock where the fluid pressure directly affects the effective stresses. Note that for this validation model we do not account for a fluid flow problem and for simplicity we basically prescribed a constant fluid pressure in the upscaled structure.

The upscaled equation for the PND approximation was then implemented in a numerical validation model example and solved using the finite element method. Additionally, the TEL approximation was also solved for and the solution of both upscaled models (PND and TEL) were compared to a full-dimensional description of the dimensionally reduced domain (reference model). A Monte Carlo simulation was performed to obtain the statistical performance and uncertainty in accuracy of the PND and TEL approximations.

3.1 Governing equations: poroelasticity

From the theory of linear poroelasticity (Biot, 1941) we have the momentum balance equation:

$$-\nabla \cdot (\boldsymbol{\sigma}) = \mathbf{f} \qquad \textit{Eq. 1}$$

where $\boldsymbol{\sigma}$ [Pa] is the total stress tensor and $\mathbf{f}$ [Pa] is the body load vector due to gravity and/or acceleration forces in dynamic problems. The poroelastic total stress tensor (here for an extensional stress regime; stress is positive in extension) is expressed as:

$$\boldsymbol{\sigma} = \boldsymbol{\sigma}_0 + \boldsymbol{\sigma}' - \alpha \Delta p \mathbf{I} \qquad \textit{Eq. 2}$$

where $\boldsymbol{\sigma}_0$ [Pa] is the initial stress, $\boldsymbol{\sigma}'$ [Pa] is the effective stress, the part of the total stress that causes deformation. The poroelastic load is expressed with Biot's coefficient α [-], typically defined as:

$$\alpha = 1 - \frac{K}{K_s} \qquad \text{Eq. 3}$$

where K_s [Pa] is the bulk modulus of the solid constituents of the porous rock. The pressure change-term in Eq. 2 describes the change in fluid pressure relative to a reference pressure p_0 [Pa]; $\Delta p = p - p_0$. The effective stress is defined as:

$$\boldsymbol{\sigma}' = \lambda \varepsilon_v \mathbf{I} + 2G\boldsymbol{\varepsilon} \qquad \text{Eq. 4}$$

Where λ [Pa] and G [Pa] are the Lamé coefficients, ε_v [-] is the volumetric strain, $\mathbf{I}$ [-] is the identity matrix and $\boldsymbol{\varepsilon}$ [-] is the strain tensor:

$$\boldsymbol{\varepsilon} = \frac{1}{2}[(\nabla\mathbf{u})^T + \nabla\mathbf{u}] \qquad \text{Eq. 5}$$

where $\mathbf{u}$ [m] is the displacement vector and the volumetric strain can be expressed as $\varepsilon_v = \nabla \cdot \mathbf{u}$. Note that the Lamé coefficients are related to the Young's modulus E [Pa] and the Poisson's ratio ν [-] by:

$$\lambda = \frac{E\nu}{(1+\nu)(1-2\nu)}, \qquad G = \frac{E}{2(1+\nu)} \qquad \text{Eq. 6}$$

To describe the poroelastic behaviour of a high-aspect ratio (HAR) structure we used two approximations, PND and TEL, that are both zero-thickness interface element-types. An important note on these zero-thickness interface element-types is that they require decoupling of the displacement variables across the interface. This is done by adding (duplicating) a minimum of one additional degree of freedom for every degree of freedom on the upscaled structure. These duplicated degrees of freedom allow the description of a discontinuous displacement on opposite sides of the interface, and they are distinguished by referring to them as the upside- and downside-component with the subscripts u and d, respectively. The two sides of the interface are then connected by force-terms that are equal in magnitude but opposite in direction and it is the description of these force-terms that distinguish the various approximations.

3.1.1 Upscaled equations: poroelastic normal deflection (PND)

The assumption behind the PND approximation is that the displacement across the thickness of the structure is varying linearly, hence the displacement vector in the HAR structure, $\mathbf{u}_r$ [m], can be expressed in terms of (1) the displacement at the upside, $\mathbf{u}_u$ [m], and (2) downside, $\mathbf{u}_d$ [m], and (3) the integration path ζ [m]:

$$\mathbf{u}_r = \mathbf{u}_d + \frac{\mathbf{u}_u - \mathbf{u}_d}{H}(\zeta - \zeta_d) \tag{Eq. 7}$$

The integration path is in the direction normal to the upscaled structure. When integrating the momentum balance equation, Eq. 1, we obtain:

$$\int_\zeta (-\nabla \cdot \boldsymbol{\sigma})\, d\zeta = \widetilde{\nabla} \cdot \boldsymbol{\Sigma} + (\boldsymbol{\sigma} \cdot \mathbf{n})|_u - (\boldsymbol{\sigma} \cdot \mathbf{n})|_d \tag{Eq. 8}$$

where $\widetilde{\nabla}$ is the tangential differential operator and the subscripts u and d are again used to describe the upside and downside of the zero-thickness HAR structure, $(\sigma \cdot \mathbf{n})$-terms are the traction forces and $\mathbf{n}$ is the normal vector. The integrated stress tensor $\boldsymbol{\Sigma}$ [Pa·m] becomes:

$$\boldsymbol{\Sigma} = \int_\zeta (\boldsymbol{\sigma})\, d\zeta = \lambda\left[\widetilde{\nabla} \cdot \mathbf{U}\right]\mathbf{I} + G\left[\widetilde{\nabla}U + \left(\widetilde{\nabla}U\right)^T\right] + \\ \lambda(\mathbf{u} \cdot \mathbf{n}|_u - \mathbf{u} \cdot \mathbf{n}|_d)\mathbf{I} + G(\mathbf{un}|_u - \mathbf{un}|_d) + G(\mathbf{nu}|_u - \mathbf{nu}|_d) - H\alpha p\mathbf{I} \tag{Eq. 9}$$

The integrated displacement vector $\mathbf{U}$ [m^2] is now expressed by:

$$\mathbf{U} = \int_\zeta (\mathbf{u}) d\zeta = \frac{\mathbf{u}|_u + \mathbf{u}|_d}{2} H \tag{Eq. 10}$$

The integrated volumetric strain E_v [m] is expressed as:

$$E_v = \int_\zeta (\varepsilon_v) d\zeta = \widetilde{\nabla} \cdot \mathbf{U} + \mathbf{u} \cdot \mathbf{n}|_u - \mathbf{u} \cdot \mathbf{n}|_d \tag{Eq. 11}$$

In summary, we can express the PND equation in a similar form as the momentum balance equation in Eq. 1 in the tangential plane of a zero thickness, high-aspect ratio structure:

$$-\widetilde{\nabla} \cdot \boldsymbol{\Sigma} = \mathbf{F} \tag{Eq. 12}$$

where we have collected the traction terms and the integral of the body load vector in $\mathbf{F}$:

$$\mathbf{F} = (\boldsymbol{\sigma} \cdot \mathbf{n})|_u - (\boldsymbol{\sigma} \cdot \mathbf{n})|_d + \int_\zeta (\mathbf{f})\, d\zeta \tag{Eq. 13}$$

3.1.2 Thin elastic layer, TEL (Goodman-type)

A common approximation of thin elastic layers is to reduce the elastic response, or poroelastic response, in a thin layer to a spring type, zero-thickness interface. The spring forces, or traction forces $\mathbf{t}_s$ [Pa] on the HAR structure depend on the relative displacement between the upside and downside of the HAR structure and act in opposite directions:

$$\mathbf{t}_{s,u} = -\mathbf{t}_{s,d} = -\frac{\mathbf{D}(\mathbf{u}_u - \mathbf{u}_d)}{H} \tag{Eq. 14}$$

where the stiffness matrix $\mathbf{D}$ [Pa] is expressed by the normal and tangential stiffness of the HAR structure:

$$\mathbf{D} = M\mathbf{nn} + G(\mathbf{I} - \mathbf{nn}) \quad \text{Eq. 15}$$

and where M [Pa] is the constrained modulus:

$$M = \frac{E(1-\nu)}{(1+\nu)(1-2\nu)} \quad \text{Eq. 16}$$

The natural boundary condition for applying a load on the faces of the HAR structure can be described as:

$$\boldsymbol{\sigma} \cdot \mathbf{n} = \mathbf{t}_s - \alpha p\mathbf{n} \quad \text{Eq. 17}$$

where p [Pa] is the fluid pressure inside the HAR structure.

3.2 Numerical models

For the validation study of the PND equation we defined a test case that challenges the typically expected capabilities of approximations of high-aspect ratio structures. The solution of the full-dimensional model was compared to the solution of the upscaled models using PND and TEL.

3.2.1 Validation model

The geometry of the validation model is shown in Fig. 1, it consists of a square geometry with sides of 400 m and a high-aspect ratio structure in the centre. The HAR structure is a sine-shaped rectangular domain with a fixed length of 100 m.

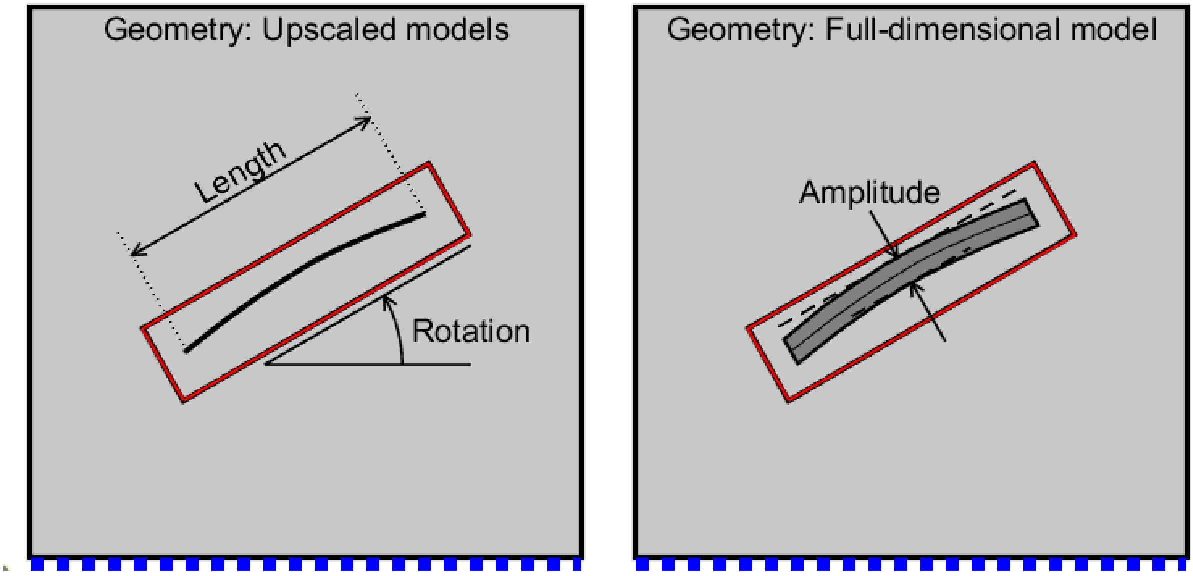

Fig. 1 *Geometry of validation models. Left: geometry used for the upscaled (PND and TEL) models (wavy black line represents the high-aspect ratio structure). Right: Model used for the full-dimensional model (dark-grey shaded area is the pressurized HAR structure, p = 1 MPa). The red rectangles indicate the locations where the solutions of the models are compared. The blue dashed lines indicate that the bottom boundary is constrained, all other outer boundaries have zero traction (free boundaries). In the figure the length of the structure is 100 m (constant, not varied in this analysis), rotation is 30°, height is 10 m and amplitude is 10 m*

In the validation study, the height, shape, and angle of the HAR structure, as well as the mechanical properties of the HAR structure and surrounding formation are varied according to Table 1.

Table 1. Properties in the validation model that are varied. Note that the Young's modulus and Poisson's ratio are varied for both the HAR structure and the surrounding formations.

Property, variable	Unit	Value	Description
Height, H	[m]	0.05-10	Height/thickness of HAR object
Rotation, R	[deg]	0-90	The angle of the HAR structure varies between 0° (horizontal) 90° (vertical) around its centre.
Amplitude, A	[m]	0-10	The HAR structure is sine-shaped with a fixed 1.5 period in the length direction and variable amplitude.
Young's modulus, E	[GPa]	0.01-10	The Young's modulus of the HAR structure (E_{up}) and surrounding formation (E_0) vary independently.
Poisson's ratio, ν	[-]	0.1-0.4	The Poisson's ratio of the HAR structure (ν_{up}) and surrounding formation (ν_0) vary independently.

Although the mechanical properties and dimensions used here are inspired by rock properties and dimensions of small-scale features relevant for a regional scale model, the methodology is also applicable to other applications, materials, and geometrical scales beyond what is demonstrated here since the problem is treated linearly poroelastic.

Because the geometry of the upscaled models and the full-dimensional model are inherently different (zero-thickness domains versus volumetric domain, respectively), the results of the three different models are compared along a perimeter around the HAR structure, as indicated by the red lines in Fig. 1.

3.3 Performance analysis: validation model

To validate and analyse the performance of the PND and TEL approximations we performed a Monte Carlo simulation. We solved many combinations of model parameters that may influence the performance of the upscaled approximations, these include geometrical and mechanical properties of the dimensionally reduced domain and the surrounding domain and compared the results from three models (two upscaled models and a full-dimensional model). The RMS (root mean square, Eq. 19) of the total displacement S [m] along a rectangular perimeter around the dimensionally reduced domain were evaluated (red dotted lines in Fig. 1) and are presented in the following section. The total displacement S is expressed as:

$$S = \sqrt{\sum_{i=1}^{N} u_i^2} \qquad \textit{Eq. 18}$$

where u_i [m] is the cartesian displacement component in direction i in N-dimension. The RMS of the error is calculated using:

$$\mathrm{RMS} = \sqrt{\frac{1}{n}\sum_{i=1}^{n}\left(\frac{Y_i - y_i}{w_i}\right)^2} \qquad \textit{Eq. 19}$$

Here Y is the solution variable (total displacement S) of the upscaled model and y is the solution variable from the full-dimensional model. The weighting number w_i is ideally equal to y_i, then the RMS will be a direct measure of accuracy, but to avoid division by a very small number, and artificially blow up the RMS-value, the weighting number is here chosen to be the mean of y_i along the comparison perimeter (red rectangle in Fig. 1). The RMS is thus an approximate measure of the error, or more precisely, an approximate measure of inaccuracy; the lower RMS, the more accurate the upscaled models are. RMS of zero would indicate zero inaccuracy, or identical solutions for the upscaled and full-dimensional models.

4 Results

The main questions we try to answer in this paper is if the PND approximation for upscaled poroelastic structures can provide sufficient accuracy for calculation of displacement, and inherently stress, around high-aspect ratio structures. Here we solved 100000 models for various geometrical and mechanical properties of the upscaled structure and the surrounding domain as described in Table 1. For all comparisons we only show the total displacement, not individual displacement components or various stress-components as the results will be highly dependent on the orientation of the HAR structure.

In Fig. 2 we compare the RMS for the total displacement for the TEL (left) and the PND (right) for various aspect ratios for the HAR structure (thickness H, varies between 0.05-10 m, divided by length L, which is constant and 100 m). In Fig. 2 the colour corresponds to the $\log_{10}$ of the stiffness ratio between the surrounding domain (E_0) and the upscaled domain (E_{up}), noting that both E_0 and E_{up} varies between 10 MPa and 10 GPa. The red colour indicates here a soft HAR (high E_{up}) compared to the surrounding domain (E_0), and for this case it can be seen in Fig. 2 that both methods are relatively accurate with a low RMS. For the case of stiff HAR (blue coloured dots), the RMS of TEL spreads widely compared to PND. This behaviour is also shown in Fig. 3.

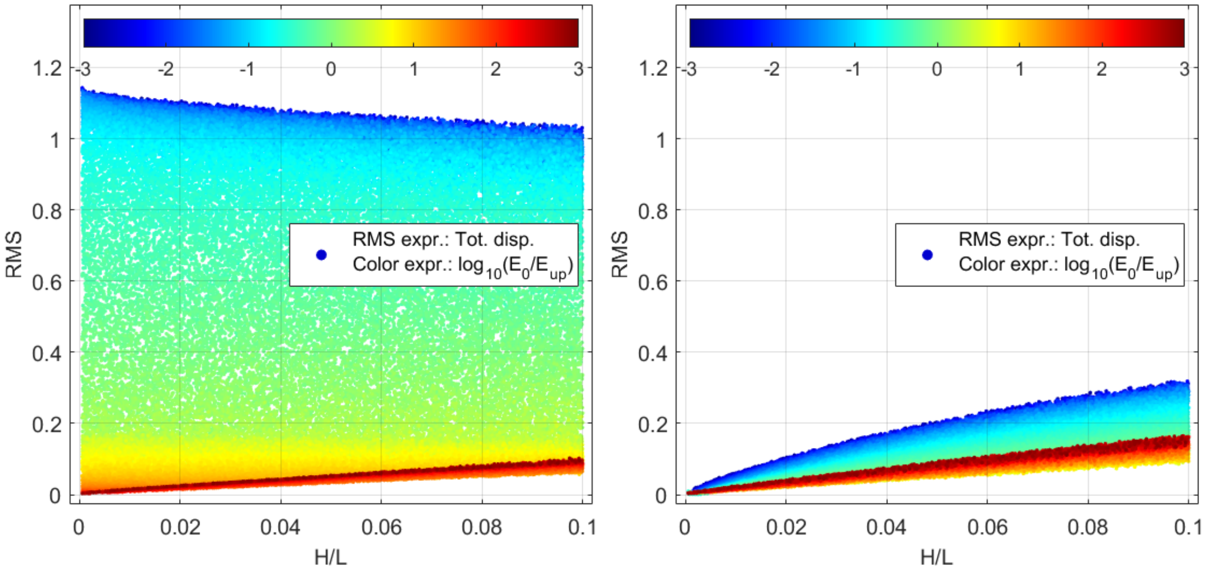

__Fig. 2__ RMS (from Eq. 19) for total displacement for the TEL (left) and the PND (right). The x-axis is the aspect ratio, the colour is the ratio of the stiffness of the surrounding domain E_0 and the upscaled domain E_{up} (both E_0 and E_{up} varies between 10 MPa and 10 GPa). See also Fig. 4 for the corresponding density plot of the RMS

In Fig. 3 we compare the $\log_{10}$ of the stiffness ratio between the surrounding domain (E_0) and the upscaled domain (E_{up}) for the TEL (left) and the PND (right). Both E_0 and E_{up} varies between 10 MPa and 10 GPa, hence the range of the ratio is from -3 to 3. In Fig. 3 the colour corresponds to the thickness H. As in Fig. 2, for a stiff HAR, or a low value of $\log_{10}(E_0/E_{up})$, the RMS of TEL increases sharply compared to PND.

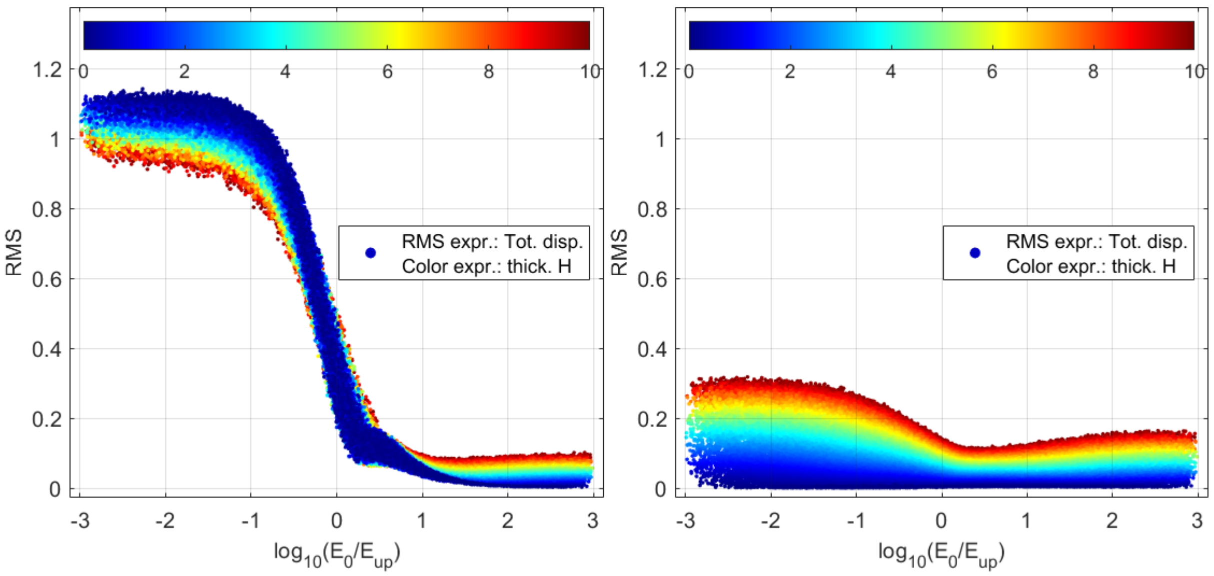

Fig. 3 *RMS (from Eq. 19) for total displacement for the TEL (left) and the PND (right). The x-axis is the ratio of the stiffness of the surrounding domain E_0 and the upscaled domain E_{up}. The colour is the thickness H. See also Fig. 5 for the corresponding density plot of the RMS*

Fig. 2 and Fig. 3 are scatter plots and the size of the markers can obscure data points that are similar. Therefore, to compensate for the lack of perspective on the data-points, a density plot (three-dimensional histogram) of Fig. 2 is shown in Fig. 4 and of Fig. 3 in Fig. 5.

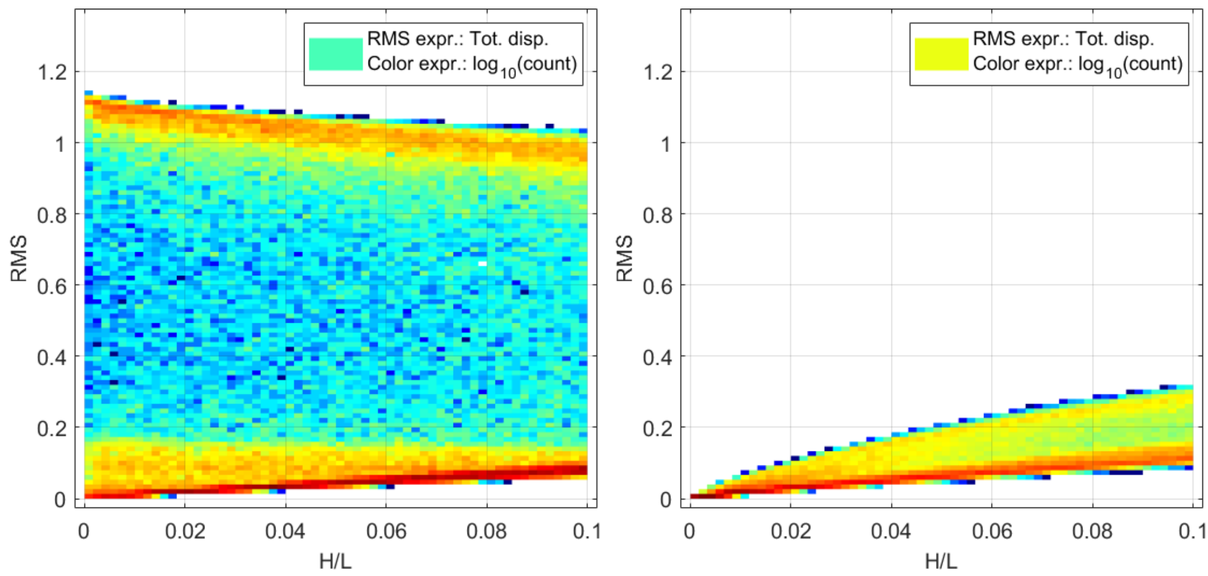

Fig. 4 *Density plot (three-dimensional histogram) of data-points in Fig. 2. Cold (blue) and hot (red) colours indicate low and high density, respectively. Note that total number of samples is 100000*

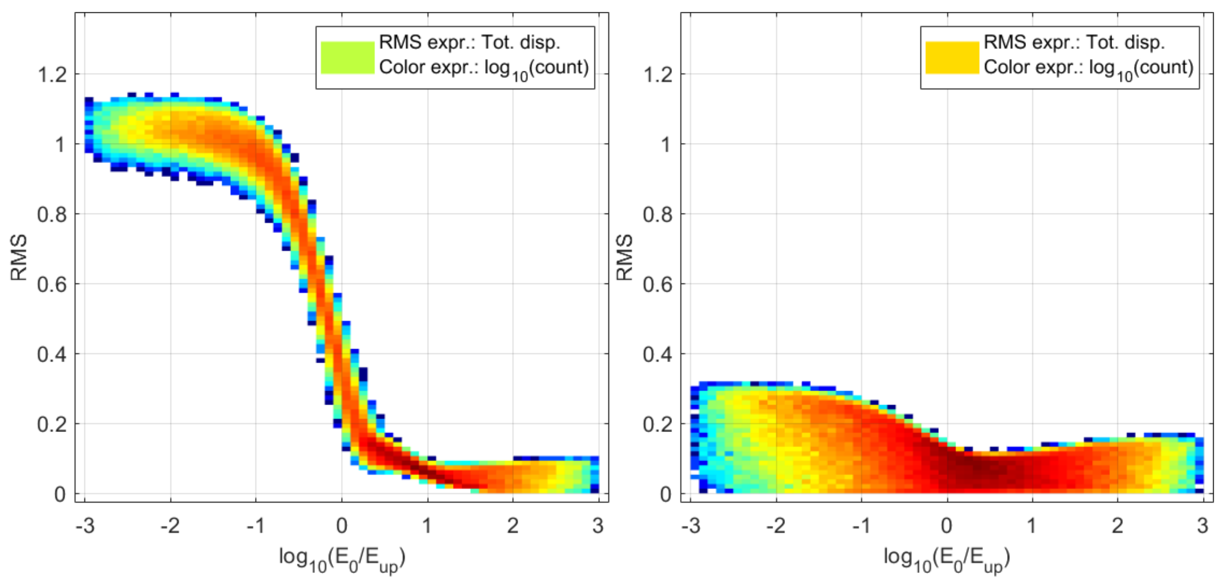

Fig. 5 Density plot (three-dimensional histogram) of data-points in Fig. 3. Cold (blue) and hot (red) colours indicate low and high density, respectively. Note that total number of samples is 100000

Density plot (three-dimensional histogram) of all the tested variables is shown in Fig. 6 for the upscaled models.

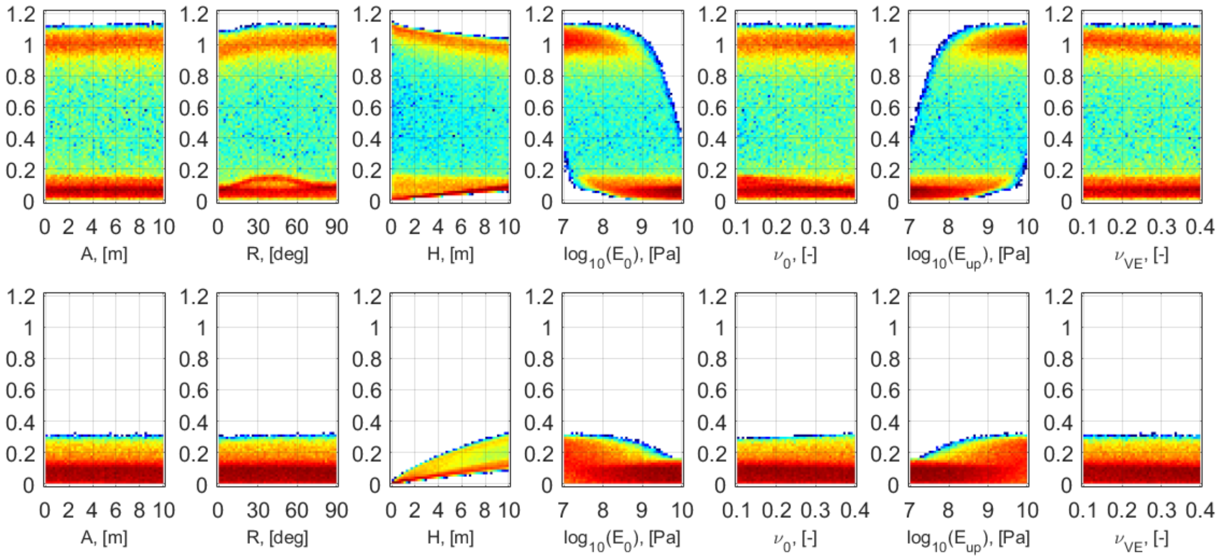

***Fig. 6** Density plot (three-dimensional histogram) of the RMS value for all the tested variables for the upscaled models: TEL in the top row and PND in the bottom row*

When correlating RMS directly to the various geometrical and mechanical properties the only clear leading-order property is the thickness of the upscaled structure for PND, see Fig. 6 (bottom). The RMS for the TEL is more complex but shows a clear correlation when considering the stiffness ratio, E_0/E_{up} in Fig. 3 and Fig. 5.

Fig. 7 shows the RMS-ratio of TEL and PND for the aspect ratio (H/L, left figure) and log10 of stiffness ratio (E_0 / E_{up}, right figure). Above the black horizontal lines in the figure the PND approximation is most accurate and below the black lines the TEL is most accurate.

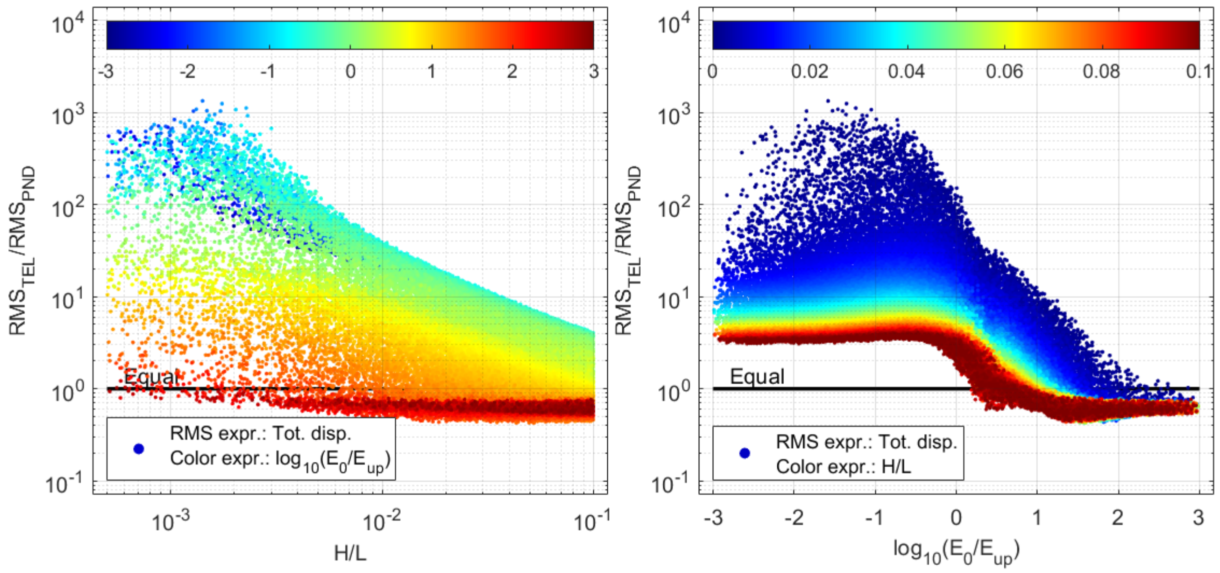

Fig. 7 *Comparing (ratio) RMS for TEL and PND for aspect ratio (H/L, left) and log$_{10}$ of stiffness ratio (E_0/E_{up}, right). The colour expressions are reversed in the figures (see legend)*

5 Discussion

To evaluate the performance of a PND approximation of high-aspect ratio structures, a validation model was defined and solved for. To test the robustness and accuracy of PND it was compared to another typically used approximation (TEL) and a full-dimensional description. Here we discuss the differences in accuracy and the leading-order effects for the performance of the tested approximations (PND and TEL).

The results show that the PND approximation is more robust for a wider range of parameters compared to the TEL. Considering the results in Fig. 2 and Fig. 7 (left) is can be seen that for the range of aspect ratio tested, 0.0005 to 0.1, the PND shows in general a higher accuracy (RMS below and up to 0.3) compared to TEL (RMS below and up to 1.2). In the context of faults and fractures, typical scaling attributes between length and thickness (equivalent to aspect ratio) are about 2 orders for faults (Torabi and Berg, 2011; Alaei and Torabi, 2017), and between length and aperture for fractures are about 2-3 orders of magnitude (Dichiarante et al. 2020). We note that the RMS, calculated from Eq. 19, is not an exact but approximate expression of the error, or deviation between the upscaled models and the reference model (full-dimensional description of the upscaled domain).

It was further found that for the PND approximation, the leading-order effects on the performance was the thickness of the high aspect-ratio domain, c.f. right Fig. 2. Another noticeable distinction of the leading order effect for the PND approximation is the stiffness ratio. It can be seen in Fig. 3 (right) that the RMS is slightly lower when the upscaled structure is softer compared to the surrounding formations.

The leading-order effects on the performance of the TEL approximation is related to the ratio of the stiffness between the high aspect-ratio object and the surrounding formations, c.f. left Fig. 3. The TEL performs well, and better than the PND approximation, when the upscaled structure is softer compared to the surrounding formations. It can be further seen in Fig. 3 that there is a correlation between the RMS for stiffness ratio (E_0/E_{up}) and thickness (H), although less significant: high stiffness ratio favours low thickness, while low stiffness ratio (E_0/E_{up}) favours high thickness, the latter is a little counter intuitive.

The simplicity of TEL is attractive, as it can be described by boundary forces and only requires splitting and decoupling of the degrees of freedom along the upscaled structure. If there are M degrees of freedom along an upscaled structure, then TEL requires $2M$ degrees of freedom while PND require $3M$ degrees of freedom. For example, in the validation model used here, the reference model that is using a full-dimensional high-aspect ratio structure (Fig. 8, right, cyan outline) has 20286 DOFs (degrees of freedom). Of the total number of DOFs, $M \approx 200$ DOFs are located on the dimensionally reduced domain (TEL and PND, Fig. 8, middle, magenta curve). This illustrates the effectiveness of the upscaling method, namely that the upscaled domains represent details in a model with a modest contribution to the total number of DOFs.

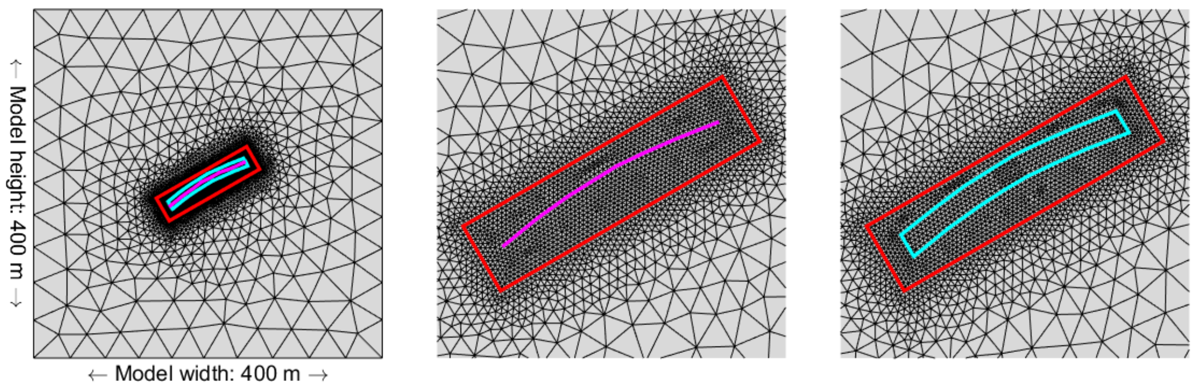

Fig. 8 *Calculation grid in model. Left: Overview of mesh in all three models, the red rectangle indicates the location where the solutions of the models are compared, cyan curves outline the full-dimensional model (dark-grey shaded area in Fig. 1, right) and magenta curve indicate the high-aspect ratio structure (TEL and PND). Centre: Close-up of high-aspect ratio structure (TEL and PND). Right: Close-up of full-dimensional high-aspect ratio structure. In the figure the length of the structure is 100 m, rotation is 30°, height is 10 m and amplitude is 10 m (see also Fig. 1)*

A significant limiting factor when using TEL compared to PND is the strong reduction in accuracy when the stiffness of the upscaled domain is higher than the surrounding formations (low E_0/E_{up}) where the error in TEL is up to 1000 times larger than PND, see Fig. 7. The elevated accuracy of the PND compared to TEL is because PND has the additional degrees of freedom (increase from $2M$ to $3M$ number of DOFs).

In this manuscript we approximate the geomechanical response in the HAR structure by linearising the displacement, going from $2M$ to $3M$ degrees of freedom, however, a higher order approximation can be obtained by adding more degrees of freedom, e.g., doubling to $6M$ degrees of freedom to a quadratic approximating of the displacement across the thickness of the upscaled structure (if linear approximation is insufficient). Another implication is that complex structures such as multi-layered structures can be upscaled by adding degrees of freedom for each virtual layer in the upscaled domain, remembering that the upscaled domain is collapsed to a lower-dimensional object.

As can be seen in the analysis here, the TEL approximation can be a good approximation when the HAR object is soft compared to surrounding formations, but in the opposite case the accuracy becomes drastically reduced. An example of the former is a hydraulically active fault in basement rock, while an example of the latter is deformation bands in porous sandstone. The benefit of PND is that the accuracy does not break down when upscaled domain becomes stiff compared to the surroundings, and the accuracy mainly depends on the geometric aspect ratio: thickness to length ratio. High robustness in the HAR structure approximation is particularly import when the stiffness is unknown a priori, for instance during an inversion of geomechanical properties.

6 Conclusion

The objective of this paper is to validate the performance and accuracy of a poroelastic normal deflection zero-thickness interface element (PND) when approximating high-aspect ratio (geo-) mechanical structures. We performed a Monte Carlo simulation (100000 models) where we varied several mechanical and geometrical properties and compared the results from using PND to a full-dimensional description of a high-aspect ratio structure (reference solution) and a commonly used approximation (a thin elastic layer, a Goodman-type zero-thickness interface element, TEL).

We found that the PND is a robust description of a high-aspect ratio structure with a low error compared to a full-dimensional description and up to 1000 times more accurate than TEL. We note that the calculated deviation between the upscaled models and the reference model (full-dimensional description of the upscaled domain) is not an exact measure of the error, but an approximate expression, because the approximations are geometric simplification, and a direct spatial comparison is therefore not possible. When considering slender structures with an aspect ratio of less than 5% (fractures and faults are typically <0.1-1%), the error was found to always be (for the wide range of tested parameters) less than 20 % but generally less than 10 % compared to the reference solution. TEL can perform well, even better than PND in some cases (when the upscaled structure is softer than surroundings) but is sensitive to the mechanical properties of the upscaled structure and the accuracy breaks down when the surrounding formations are softer than the upscaled structure, regardless of the tested thickness, shape, and rotation.

The elevated accuracy from the PND-method comes from the addition of extra degrees of freedom, but the number of added degrees is relatively low compared to the total size of the problem of which the upscaled structures is a part of. Compared to TEL, we find that the PND is a more robust approximation for high-aspect ratio structures, it requires only a minor modification to any numerical code that already support TEL and represents only a marginal increase in model size.

7 Acknowledgment

SENSE (Assuring integrity of CO_2 storage sites through ground surface monitoring) project No. 299664, has been subsidized through ACT (EC Project no. 691712) by Gassnova, Norway, United Kingdom Department for Business, Energy and Industrial Strategy, Forschungszentrum Jülich GMBH, Projektträger Jülich, Germany, The French Agency for the Environment and Energy Management, The United States Department of Energy, and State Research Agency, Spain. Additional support from Equinor and Quad Geometrics and permission to use data from the Krechba Field by In Salah Gas JV are appreciated.

8 Statements and Declarations

The authors have no financial or proprietary interests in any material discussed in this article.

9 References

Alaei, B. and Torabi, A. (2017). Seismic imaging of fault damaged zone and its scaling relation with displacement. Interpretation, 5(4):SP83–SP93.

Bear, J. and Corapcioglu, M. Y. (1981a). Mathematical Model for Regional Land Subsidence Due to Pumping: 1. Integrated Aquifer Subsidence Equations Based on Vertical Displacement Only. Water Resources Research, 17(4):937–946.

Bear, J. and Corapcioglu, M. Y. (1981b). Mathematical Model for Regional Land Subsidence Due to Pumping: 2. Integrated Aquifer Subsidence Equations for Vertical and Horizontal Displacements. Water Resources Research, 17(4):947–958.

Biot, M. A. (1941). General Theory of Three-dimensional Consolidation. Journal of Applied Physics, 12(2):155–164.

Bjørnarå, T. I., Nordbotten, J. M., and Park, J. (2016). Vertically integrated models for coupled two-phase flow and geomechanics in porous media. Water Resources Research, 52(2):1398–1417.

Bjørnarå, T. I., Park, J., and Jostad, H. P. (2021). Hydraulic fracturing numerical simulation: micro-seismicity and fluid-type dependency. In Proceedings of the 15th Greenhouse Gas Control Technologies Conference 15-18 March 2021 (GHGT-15).

Camanho, P. P. and Hallett, S. R. (2015). Numerical modelling of failure in advanced composite materials. Woodhead Publishing.

Corapcioglu, M. Y. and Bear, J. (1983). A Mathematical Model for Regional Land Subsidence Due to Pumping: 3. Integrated Equations for a Phreatic Aquifer. Water Resources Research, 19(4):895–908.

Dichiarante, A. M., McCaffrey, K. J. W., Holdsworth, R. E., Bjørnarå, T. I., and Dempsey, E. D. (2020). Fracture attribute scaling and connectivity in the devonian orcadian basin with implications for geologically equivalent subsurface fractured reservoirs. Solid Earth, 11(6):2221–2244. 1

Fredman, N., Tveranger, J., Semshaug, S., Braathen, A., and Sverdrup, E. (2007). Sensitivity of fluid flow to fault core architecture and petrophysical properties of fault rocks in siliciclastic reservoirs: a synthetic fault model study. Petroleum Geoscience, 13(4):305–320.

Gasda, S. E., Nordbotten, J. M., and Celia, M. A. (2011). Vertically averaged approaches for CO2 migration with solubility trapping. Water Resources Research, 47. W05528.

Goodman, R. E., Taylor, R. L., and Brekke, T. L. (1968). A model for the mechanics of jointed rock. Journal of the soil mechanics and foundations division, 94(3):637–659.

Grant, N. T. (2020). Stochastic modelling of fault gouge zones: implications for fault seal analysis. Geological Society, London, Special Publications, 496(1):163–197.

Kolyukhin, D. and Tveranger, J. (2015). Statistical modelling of fault core and deformation band structure in fault damage zones. In 77th EAGE Conference and Exhibition 2015, pages 1–5. European Association of Geoscientists & Engineers.

Lutome, M. S., Lin, C., Chunmei, D., Zhang, X., and Bishanga, J. M. (2021). 3D geocellular modeling for reservoir characterization of lacustrine turbidite reservoirs: Submember 3 of the third member of the Eocene Shahejie Formation, Dongying depression, Eastern China. Petroleum Research.

Nordbotten, J. M., Celia, M. A., and Bachu, S. (2005). Injection and storage of CO2 in deep saline aquifers: Analytical solution for CO2 plume elvolution during injection. Transp. Porous Med., 58:339–360.

Torabi, A. and Berg, S. S. (2011). Scaling of fault attributes: A review. Marine and Petroleum Geology, 28(8):1444–1460.